Granular Matter (2009) 11:331–343
DOI 10.1007/s10035-009-0146-2

A finite deformation method for discrete modeling: particle rotation and parameter calibration

Yucang Wang · Fernando Alonso-Marroquin

Received: 29 February 2008 / Published online: 10 June 2009

Abstract We present a finite deformation method for 3-D discrete element modeling. In this method particle rotation is explicitly represented using quaternion and a complete set of interactions is permitted between two bonded particles, i.e., normal and tangent forces, rolling and torsional torques. Relative rotation between two particles is decomposed into two sequence-independent rotations, such that an overall torsional and rolling angle can be distinguished and torques caused by relative rotations are uniquely determined. Forces and torques are calculated in a finite deformation fashion, rather than incrementally. Compared with the incremental methods our algorithm is numerically more stable while it is consistent with the non-commutativity of finite rotations. We study the macroscopic elastic properties of a regularly arranged 2-D and 3-D lattice. Using a micro-to-macro approach based on the existence of a homogeneous displacement field, we study the problem of how to choose the particle-scale parameters (normal, tangent, rolling and torsional stiffness) given the macroscopic elastic parameters and geometry of lattice arrangement. The method is validated by reproducing the wing crack propagation and the fracture patterns under uniaxial compression. This study will provide a theoretical basis for the calibration of the DEM parameters required in engineering applications.

Y. Wang (✉)
CSIRO Exploration and Mining, PO Box 883,
Kenmore, Brisbane, QLD 4069, Australia
e-mail: Yucang.Wang@csiro.au; yucang_wang@hotmail.com

F. Alonso-Marroquin
MoSCoS, School of Mathematics and Physics,
The University of Queensland, St Lucia, Brisbane,
QLD 4072, Australia
e-mail: fernando@physics.uq.edu.au

Keywords Discrete element method · The ESyS_particle · Decomposition of finite rotation · Quaternion · FCC · HCP

1 Introduction

The discrete element method (DEM), pioneered by Cundall [1], is a powerful numerical tool that is extensively used in many scientific and engineering problems. The basic idea behind DEM is to represent the material to be modeled as an assemblage of discrete particles interacting with one another. The precise nature of the interaction depends on the scale of interest and the details of the simulation. At each time step, the calculations performed in DEM alternate between integrating equations of motion for each particle, and applying the force-displacement law at each contact, which updates the contact forces based on the relative motions between two particles and their relevant contact stiffnesses.

In DEM simulations, there are three important issues, which play a very important role and greatly affect the simulation results: (1) The adoption of the force-displacement law; (2) The method to update the interparticle interactions; and (3) The correct choice of the microscopic parameters to reproduce experimental data.

As regards the force-displacement law, different DEMs employ different relationships, depending on what kind of interaction is transmitted [2]. One kind of DEM permits the neighboring particles to be bonded together by springs through which both attractive and repulsive forces can be transmitted [3–19]. Among these bonded models, some simple models only include normal forces between particles [3–8]. Other models consider normal and tangent forces but prohibit single particle rotations [9–11,18]. The main reason to hinder rotation is to eliminate the effect of rolling, which leads to bulk frictions much lower than those observed in

real granular materials [20]. However, numerous studies from experiments and numerical simulations suggest that rolling resistance at contacts has a significant influence on behavior of granular media [21–27]. These observations imply that at least in certain cases, particle rotations and rotational stiffnesses can not be ignored. For these reasons full degrees of freedom and the complete set of interactions needs to be implemented to capture the overall dynamics of granular materials.

If a DEM contains the complete set of interactions, the second important problem is how to calculate these interactions. In the few existing models which include the complete set of interactions [2,13,14,28], the incremental method is used to calculate forces and torques caused by relative translational motions and rotations. However, the method is accurate only when the time step is taken small enough. For larger time steps, incremental methods lose accuracy because 3-D finite rotations are non-commutative. Those errors can also accumulate over time, leading to spurious path dependency of the elastic energy. In this paper we introduce a method where contact forces and torques are calculated from finite displacement and finite particle rotation. We show that the method reduces the sensitivity of the simulations on time steps.

The third important issue we need to consider is how to choose the contact stiffness parameters in order to get realistic macroscopic results. In most DEM simulations, values for the micro-physical elastic stiffness parameters are typically chosen via empirical or trial-and-error methods [9–11,29,30]. People from outside the DEM community sometimes have the wrong impression that DEM parameters are chosen arbitrarily and the DEM does not generate the realistic macroscopic elasticity, as continuum models (such as the finite element method) do. Therefore a theoretical study about the choice of the stiffnesses is much needed and it is desirable to derive the relationship between the particle scale stiffness parameters (which characterize these interactions) and the macroscopic elastic constants of the materials. Some attempts have been made along this direction. For example, elasticity of randomly packed granular material can be found in [31,32]. Elastic properties of 3-D regular packing of elastic spheres were calculated in [33–36]. However particle rotation and rotational stiffnesses were not taken into account in these studies. The effect of particle rotation was considered by Chang et al. [37] using a random packing. An extra group of parameters was needed since their focus is on the materials with strong micro-polar effect. In this paper we derive the macroscopic elasticity parameters for 2D and 3D regular packing in terms of the microscopic contact parameters, taking into account the overall effects of particle rotations.

The paper is organized as follows: In Sect. 2 we present the model and the way of calculating forces and torques based on the state-of-art algorithm of decomposing finite rotations; in Sect. 3 we derive a relationship between the spring constants and macroscopic elastic constants in case of identical spherical particles arranged in regular lattices. Section 4 gives some numerical validations, followed by discussions and conclusions in Sect. 5.

2 Model

The model presented in this paper was implemented into the ESyS_Particle platform. The ESyS_Particle, previously called Lattice Solid Model or LSMearth, was motivated by the Molecular Dynamics [38,39] but particle interactions are specified to simulate the micro-mechanical behavior of rocks [3–7]. It is similar in principle to the DEM to model granular assemblages [1]. The ESyS_Particle has been applied to the study of physical processes such as rock fracture [4,7], stick-slip friction behavior [4,6], granular dynamics and heat-flow paradox [5,40], localization phenomena [41], load-unload response ratio theory [42,43] and critical point systems [44].

In this DEM implementation presented here a full set of interactions is involved, that is, all three interactions (normal, tangent forces and rolling torques) in 2-D and six (normal, tangent forces, rolling and torsional torques) in 3-D are transmitted between bonded particles. Here we introduce a different technique that has been developed to decompose the finite relative rotations between two rigid bodies in such a way that the torques and forces caused by such relative rotations can be uniquely determined.

2.1 The equations of particle motion

Particle motion can be decomposed into two completely independent parts, translational motion of the center of mass and rotation about the center of mass. The former is governed by the Newtonian equation

$$\ddot{\boldsymbol{r}}(t) = \boldsymbol{f}(t)/M, \tag{1}$$

where $\boldsymbol{r}(t)$ and M are position of the particle and the particle mass respectively. $\boldsymbol{f}(t)$ is the total forces acting on the particle, which may include the spring forces by the neighboring particles (given in Eq. (20)), the forces by the walls, viscous force, gravitational force etc. The equation above can be integrated using the velocity Verlet scheme [4,6,38].

The particle rotation depends on the total applied torque and usually involves two coordinate frames, one is fixed in space, called space-fixed frame, in which Eq. (1) is applied. The other is attached to the principal axes of the rotation body, referred to as body-fixed frame. The particle rotation is governed by the Euler's equations (in the body-fixed frame) [45]

$$\begin{aligned}\tau_x^b &= I_{xx}\dot{\omega}_x^b - \omega_y^b\omega_z^b\left(I_{yy} - I_{zz}\right)\\ \tau_y^b &= I_{yy}\dot{\omega}_y^b - \omega_z^b\omega_x^b\left(I_{zz} - I_{xx}\right)\\ \tau_z^b &= I_{zz}\dot{\omega}_z^b - \omega_x^b\omega_y^b\left(I_{xx} - I_{yy}\right)\end{aligned} \tag{2}$$

where τ_x^b, τ_y^b and τ_z^b are components of total torque $\boldsymbol{\tau}^b$ expressed in body-fixed frame, ω_x^b, ω_y^b and ω_z^b are components of angular velocities $\boldsymbol{\omega}^b$ measured in body-fixed frame, and I_{xx}, I_{yy} and I_{zz} are the three principle moments of inertia in body-fixed frame in which the inertia tensor is diagonal. In case of 3-D spheres, $I = I_{xx} = I_{yy} = I_{zz}$.

In our model, the unit quaternion $q = q_0 + q_1 i + q_2 j + q_3 k$ is used to explicitly describe the orientation of each particle [46,47]. The physical meaning of a quaternion is that it represents a one-step rotation around the vector $q_1\hat{i} + q_2\hat{j} + q_3\hat{k}$ with a rotation angle of $2\mathbf{arccos}(q_0)$ [48]. A quaternion for each particle satisfies the following equation [46,47],

$$\dot{\boldsymbol{Q}} = \frac{1}{2}\boldsymbol{Q}_0(q)\boldsymbol{\Omega},$$

$$\text{where } \dot{\boldsymbol{Q}} = \begin{pmatrix}\dot{q}_0\\ \dot{q}_1\\ \dot{q}_2\\ \dot{q}_3\end{pmatrix}, \boldsymbol{Q}_0(q) = \begin{pmatrix}q_0 & -q_1 & -q_2 & -q_3\\ q_1 & q_0 & -q_3 & q_2\\ q_2 & q_3 & q_0 & -q_1\\ q_3 & -q_2 & q_1 & q_0\end{pmatrix},$$

$$\boldsymbol{\Omega} = \begin{pmatrix}0\omega_x^b\\ \omega_y^b\\ \omega_z^b\end{pmatrix}. \tag{3}$$

Detailed algorithms to solve Eqs. (2)–(3) can be found in Wang et al. [49,50].

2.2 Contact laws, particle interactions and calculation of forces and torques

Three kinds of interactions exist between contact particles in the current ESyS_Particle model: bonded, solely normal repulsive and cohesionless frictional interaction. Bonded interactions between particles in contact allow transmission of tensile forces, which can be used to model behaviors of continuum or intact materials. The breakage of bonds provides an explicit mechanism for microscopic fracture. This is different from the solely normal repulsive and cohesionless frictional interaction, which does not allow tensile forces to be transmitted between particles.

2.2.1 Bonded interaction

For bonded interactions, the three important issues that need to be specified are types of interactions being transmitted between each particle pair, the algorithm to calculate the interactions between bonded particles due to the relative motion and the criterion for a bond to break.

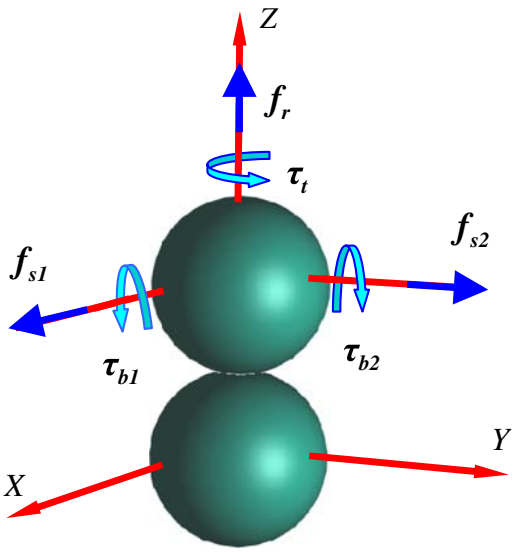

Fig. 1 Six kinds of interactions between bonded particles. f_r is normal force, f_{s1} and f_{s2} are tangent forces, τ_t is torsional torque, τ_{b1} and τ_{b2} are rolling torque

The force-displacement law and interactions transmitted Theoretically, six independent parameters are required to represent a 3-D particle, thus six kinds of relative motions exist between two bonded particles. We hope that the relationship between interactions and relative displacements between two bonded particles can be written in the linear form (Fig. 1)

$$\begin{aligned}&\boldsymbol{f}_r = K_r\Delta\boldsymbol{r}, \quad \boldsymbol{f}_{s1} = K_{s1}\Delta\boldsymbol{s}_1 \quad \boldsymbol{f}_{s2} = K_{s2}\Delta\boldsymbol{s}_2,\\ &\boldsymbol{\tau}_t = K_t\Delta\boldsymbol{\alpha}_t, \quad \boldsymbol{\tau}_{b1} = K_{b1}\Delta\boldsymbol{\alpha}_{b1}, \quad \boldsymbol{\tau}_{b2} = K_{b2}\Delta\boldsymbol{\alpha}_{b2},\end{aligned} \tag{4}$$

where $\Delta\boldsymbol{r}$, $\Delta\boldsymbol{s}_1$ ($\Delta\boldsymbol{s}_2$)are the relative displacements in normal and tangent directions. $\Delta\boldsymbol{\alpha}_t$ and $\Delta\boldsymbol{\alpha}_{b1}$ ($\Delta\boldsymbol{\alpha}_{b2}$) are the relative angular displacements caused by torsion and rolling. $\boldsymbol{f}_r, \boldsymbol{f}_{s1}, \boldsymbol{f}_{s2}, \boldsymbol{\tau}_t, \boldsymbol{\tau}_{b1}$ and $\boldsymbol{\tau}_{b2}$ are forces and torques, K_r, K_{s1}, K_{s2}, K_t, K_{b1} and K_{b2} are relevant stiffness. In this study we assume that the bonds are identical in every direction, $K_s = K_{s1} = K_{s2}$ and $K_b = K_{b1} = K_{b2}$. It should be pointed out that Eq. (4) is valid only for infinitesimal small deformation. In case of finite deformation, rotation series are non-commutative, or order dependent. For example, a rotation of $\Delta\boldsymbol{\alpha}_{b1}$ followed by a rotation of $\Delta\boldsymbol{\alpha}_{b2}$ leads, in principle, to a final orientation which is different when we apply $\Delta\boldsymbol{\alpha}_{b2}$ followed by $\Delta\boldsymbol{\alpha}_{b1}$. We will show that the two rolling motions, $\Delta\boldsymbol{\alpha}_{b1}$ and $\Delta\boldsymbol{\alpha}_{b2}$, actually can not be decoupled. Therefore in practice they are treated as one rolling motion, controlled by an orientation angle.

Calculation of interactions due to relative motion Before solving Eqs. (2)–(3), forces and torques due to the relative motions between bonded particles need to be calculated based on the position and orientation of each particle. We developed a Finite Deformation Method (FDM) [50] as an alternative to the incremental method [13,28]. In this method the total

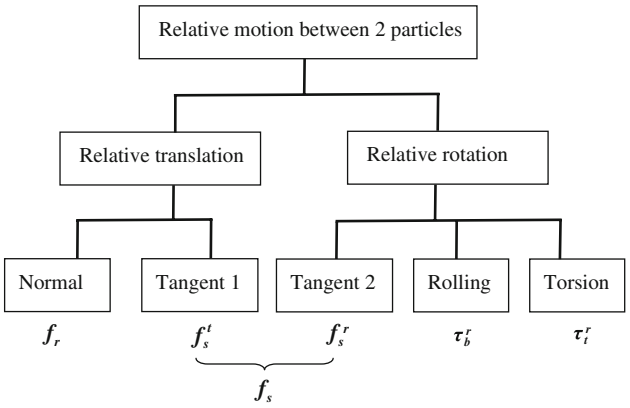

Fig. 2 The scheme of decomposing the relative motions between two particles

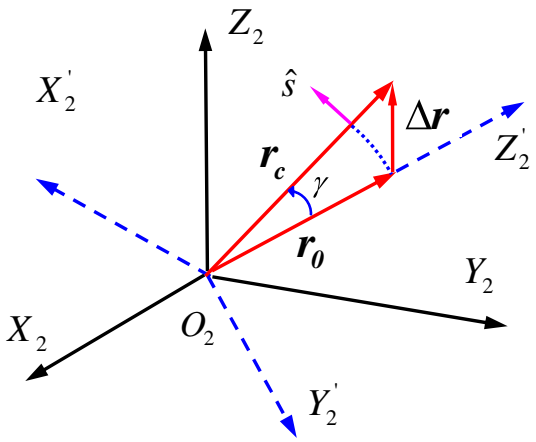

Fig. 3 The relative translational displacements of particle 1 relative to particle 2 with respect to $X_2Y_2Z_2$ co-ordinates is $\Delta \boldsymbol{r} \cdot \boldsymbol{r}_0$ and $\boldsymbol{r}_c$ are initial and current relative position of particle 1 in $X_2Y_2Z_2$

relative (translational and rotational) displacements between each pair of bonded particles are calculated at each time step. Then the forces and torques are calculated in terms of those relative displacements. The method is different in spirit from the incremental methods, where forces and torques are incremented in each time step based on those of the previous time step.

The FDM scheme requires a complete decomposition of the relative motions between particle pairs. The basic idea of the decomposition is outlined in Fig. 2. The body-fixed frame of one particle (particle 2) is taken as a reference, and the relative motion between the two particles are decomposed into relative translational motion (without relative rotation) and relative rotation (without translation). The two parts are completely independent. Then the translation is decomposed into normal and tangent motions. To decompose the relative rotation, a two-step decomposition scheme is developed in which torsion (or twisting) and rolling (or rolling) are fully decoupled and order-independent [50]. Note that the relative rotation may contribute to tangent motions. The detailed algorithm is described below.

Suppose in the space-fixed frame, the initial positions of particle 1 and 2 at time $t = 0$ are $\boldsymbol{r}_{10} = x_{10}\boldsymbol{i} + y_{10}\boldsymbol{j} + z_{10}\boldsymbol{k}$ and $\boldsymbol{r}_{20} = x_{20}\boldsymbol{i} + y_{20}\boldsymbol{j} + z_{20}\boldsymbol{k}$, the initial orientations of particle 1 and 2 are $p^0 = 1 + 0i + 0j + 0k$ and $q^0 = 1 + 0i + 0j + 0k$. At time t, the current positions are $\boldsymbol{r}_1 = x_1\boldsymbol{i} + y_1\boldsymbol{j} + z_1\boldsymbol{k}$ and $\boldsymbol{r}_2 = x_2\boldsymbol{i} + y_2\boldsymbol{j} + z_2\boldsymbol{k}$, the current orientations are $p = p_0 + p_1 i + p_2 j + p_3 k$ and $q = q_0 + q_1 i + q_2 j + q_3 k$. Let $X_1Y_1Z_1$ and $X_2Y_2Z_2$ represent the body-fixed frame of particle 1 and 2, the relative translational displacements of particle 1 with respect to $X_2Y_2Z_2$ is (Fig. 3)

$$\Delta \boldsymbol{r} = \boldsymbol{r}_c - \boldsymbol{r}_0, \tag{5}$$

where

$$\boldsymbol{r}_0 = \boldsymbol{r}_{10} - \boldsymbol{r}_{20} = x_{12}\boldsymbol{i} + y_{12}\boldsymbol{j} + z_{12}\boldsymbol{k}, \tag{6}$$

is the initial position of particle 1 relative to particle 2 and r_c, the current position of particle 1 relative to particle 2 (measured in $X_2Y_2Z_2$), is determined by

$$\boldsymbol{r}_c = q^{-1}\boldsymbol{r}_f q, \tag{7}$$

where $\boldsymbol{r}_f = \boldsymbol{r}_1 - \boldsymbol{r}_2$.

The normal force acting on particle 2 becomes

$$\boldsymbol{f}_r = K_r \left(|\boldsymbol{r}_c| - |\boldsymbol{r}_0|\right) \boldsymbol{r}_c / |\boldsymbol{r}_c|. \tag{8}$$

The tangent force acting on particle 2 has two contributions

$$\boldsymbol{f}_s = \boldsymbol{f}_s^t + \boldsymbol{f}_s^r, \tag{9}$$

where

$$\boldsymbol{f}_s^t = K_s \, |\boldsymbol{r}_0| \, \gamma \hat{\boldsymbol{s}}, \tag{10}$$

is caused by the translational tangent displacement ($|\boldsymbol{r}_0| \, \gamma$) of particle 1 relative to $X_2Y_2Z_2$ without relative rotation. The angle γ is determined by $\mathbf{cos}\gamma = \boldsymbol{r}_0 \cdot \boldsymbol{r}_c / |\boldsymbol{r}_0| \, |\boldsymbol{r}_c|$ and the direction of $\boldsymbol{f}_s^t$ is determined by unit vector $\hat{\boldsymbol{s}} = \boldsymbol{r}_c \times (\boldsymbol{r}_c \times \boldsymbol{r}_0) / |\boldsymbol{r}_c \times (\boldsymbol{r}_c \times \boldsymbol{r}_0)|$.

Since $\boldsymbol{f}_s^t$ is exerted on the contact surface of the two particles, rather than the center of particle 2, it generates a torque

$$\boldsymbol{\tau}_s^t = \frac{1}{2} \, |\boldsymbol{r}_c| \, \left| \boldsymbol{f}_s^t \right| \hat{\boldsymbol{t}}, \tag{11}$$

where the unit vector $\hat{\boldsymbol{t}} = \boldsymbol{r}_0 \times \boldsymbol{r}_c / |\boldsymbol{r}_0 \times \boldsymbol{r}_c|$ specifies the direction of $\boldsymbol{\tau}_s^t$. Note that Eqs. (8), (10) and (11) are evaluated in $X_2Y_2Z_2$co-ordinates.

$\boldsymbol{f}_s^r$ in Eq. (9), caused by relative rotation of particle 1 with respect to $X_2Y_2Z_2$, is given later in Eqs. (16) and (18).

The relative rotation of particle 1 over particle 2, or rotation from $X_2Y_2Z_2$ to $X_1Y_1Z_1$, is represented by the quaternion $g^o = q^{-1}p = q^*p$ (expressed in $X_2Y_2Z_2$). Let $X'_2Y'_2Z'_2$ be an auxiliary frame, obtained by directly rotating $X_2Y_2Z_2$ such that its Z'_2-axis is pointing to particle 1 at

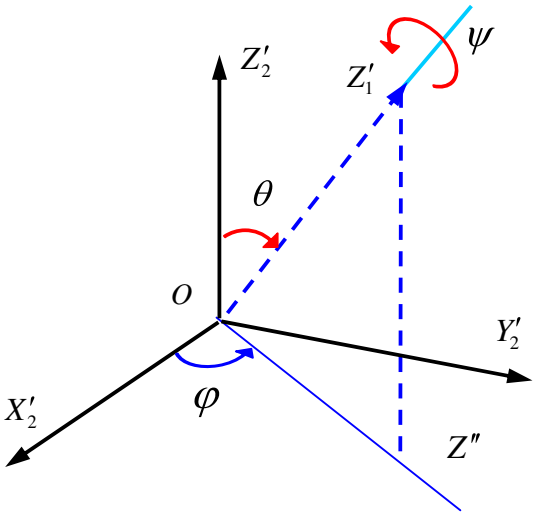

Fig. 4 An arbitrary rotation between two rigid bodies or two coordinate systems can be decomposed into two-step rotations, one pure axial rotation of angle ψ around its Z'_2-axis, and one rotation of Z'_2-axis over θ on certain plane controlled by another parameter φ

t = 0. $X'_2Y'_2Z'_2$ rotates with $X_2Y_2Z_2$ and there is no relative rotation between them. It is the $X'_2Y'_2Z'_2$ system in which we evaluate the relative rotation between two particles, which can also be expressed by the quaternion $g = h^{-1}g^o h = g_0 + g_1 i + g_2 j + g_3 k$ (expressed in $X'_2Y'_2Z'_2$ system), where the quaternion h specifies the rotation from $X_2Y_2Z_2$ to $X'_2Y'_2Z'_2$, and is given by

$$
\begin{aligned}
h_0 &= \frac{\sqrt{2}}{2}\sqrt{\frac{\sqrt{x_{12}^2+y_{12}^2+z_{12}^2}+z_{12}}{\sqrt{x_{12}^2+y_{12}^2+z_{12}^2}}},\\
h_1 &= -\frac{\sqrt{2}}{2}\sqrt{\frac{\sqrt{x_{12}^2+y_{12}^2+z_{12}^2}-z_{12}}{\sqrt{x_{12}^2+y_{12}^2+z_{12}^2}}}\frac{y_{12}}{\sqrt{x_{12}^2+y_{12}^2}},\\
h_2 &= \frac{\sqrt{2}}{2}\sqrt{\frac{\sqrt{x_{12}^2+y_{12}^2+z_{12}^2}-z_{12}}{\sqrt{x_{12}^2+y_{12}^2+z_{12}^2}}}\frac{x_{12}}{\sqrt{x_{12}^2+y_{12}^2}},\\
h_3 &= 0.
\end{aligned}
\tag{12}
$$

By using quaternion algebra, it has been proved that [50] the relative rotation g cannot be decomposed into three mutually independent rotations around three orthogonal axes as expected in Eq. (4). Hopefully it can be decomposed into two independent rotations. This means that one can either start from a rotation of angle θ from Z'_2-axis to Z'_1-axis first (determined by the orientation angle φ), then followed by an axial rotation of angle ψ about Z'_1-axis (Fig. 4 corresponds to this), or change orders of the two rotations such that an axial rotation of angle ψ about Z'_2-axis is followed by a rotation of angle θ from the Z'_2-axis to the Z'_1-axis (with the orientation angle $\varphi - \psi$) [50]. These two rotations, corresponding to the relative torsion of angle ψ and rolling of angle θ between two particles in our model, are sequence-independent. Rolling can not be decomposed further.

The advantage of the sequence-independent decomposition is that it respects the physical law (3-D finite rotation series are order dependent) and the forces and torques determined by this decomposition are unique. The three independent parameters ψ, θ and φ are given by

$$
\begin{aligned}
&\cos\frac{\psi}{2} = \frac{g_0}{\sqrt{g_0^2+g_3^2}}, \quad \sin\frac{\psi}{2} = \frac{g_3}{\sqrt{g_0^2+g_3^2}},\\
&\cos\theta = g_0^2 - g_1^2 - g_2^2 + g_3^2,\\
&\cos\varphi = \frac{g_1g_3 + g_0g_2}{\sqrt{\left(g_0^2+g_3^2\right)\left(g_1^2+g_2^2\right)}},\\
&\sin\varphi = \frac{g_2g_3 - g_0g_1}{\sqrt{\left(g_0^2+g_3^2\right)\left(g_1^2+g_2^2\right)}}.
\end{aligned}
\tag{13}
$$

The decomposition of the rotation g can be mathematically expressed as

$$
\begin{aligned}
g = &\left(\cos\frac{\theta}{2} - i\sin\frac{\theta}{2}\sin\varphi + j\sin\frac{\theta}{2}\cos\varphi\right)\\
&\times\left(\cos\frac{\psi}{2} + k\sin\frac{\psi}{2}\right)
\end{aligned}
\tag{14}
$$

or

$$
\begin{aligned}
g = &\left(\cos\frac{\psi}{2} + k\sin\frac{\psi}{2}\right)\left(\cos\frac{\theta}{2} - i\sin\frac{\theta}{2}\sin(\varphi-\psi)\right.\\
&\left.+ j\sin\frac{\theta}{2}\cos(\varphi-\psi)\right).
\end{aligned}
\tag{15}
$$

Equation (14) stands for the rolling of angle θ then followed by a torsion of angle ψ, while Eq. (15) for the opposite order.

The torques and tangent forces exerted on particle 2 are (expressed in $X'_2Y'_2Z'_2$ co-ordinates)

$$
\begin{aligned}
&\boldsymbol{\tau}'_b = g'\boldsymbol{\tau}''_b g'^{-1},\\
&\boldsymbol{\tau}'_t = g'\boldsymbol{\tau}''_t g'^{-1},\\
&\boldsymbol{f}'_s = -K_s\,|\boldsymbol{r}_c|\,\theta\,(\cos\varphi\boldsymbol{i} + \sin\varphi\boldsymbol{j})/2,\\
&\boldsymbol{\tau}'_s = K_s\,|\boldsymbol{r}_c|^2\,\theta\,(\sin\varphi\boldsymbol{i} - \cos\varphi\boldsymbol{j})/4,
\end{aligned}
\tag{16}
$$

where $\boldsymbol{\tau}'_s$ is the torque generated by $\boldsymbol{f}'_s$. $\boldsymbol{\tau}''_b = K_b\theta\left(-sin\,\varphi\,\hat{\boldsymbol{i}} + cos\,\varphi\hat{\boldsymbol{j}}\right)$ is the torque caused by rolling with no torsion, and $\boldsymbol{\tau}''_t = K_t\psi\hat{\boldsymbol{k}}$ is the torsional torque without rolling, and

$$
\begin{aligned}
g' = &\left(\cos\frac{\theta}{4} - i\sin\frac{\theta}{4}\sin\varphi + j\sin\frac{\theta}{4}\cos\varphi\right)\\
&\times\left(\cos\frac{\psi}{4} + k\sin\frac{\psi}{4}\right),
\end{aligned}
\tag{17}
$$

is the rotation of the contact surface of the two particles expressed in $X'_2Y'_2Z'_2$. Equation (17) is similar to Eq. (14)

except that it is determined by parameter ($\theta/2$, $\psi/2$ and φ) instead of (θ, ψ and φ). The reason why the torques should be rotated by a rotation of g' is because rolling and torsion are coupled and they change the torque of each other when they both exist.

Torques and forces can easily be transformed back to $X_2Y_2Z_2$ frame using

$$\begin{aligned} \boldsymbol{\tau}_b^r &= h\boldsymbol{\tau}_b' h^{-1}, \quad \boldsymbol{\tau}_t^r = h\boldsymbol{\tau}'_t h^{-1}, \\ \boldsymbol{f}_s^r &= g''(h\boldsymbol{f}_s' h^{-1})g''^{-1}, \quad \boldsymbol{\tau}_s^r = g''(h\boldsymbol{\tau}'_s h^{-1})g''^{-1}, \end{aligned} \tag{18}$$

where g'' is the rotation caused by the translational tangent displacement (Eq. (10)). It is determined by a vector $\boldsymbol{v}_\gamma = \boldsymbol{r}_0 \times \boldsymbol{r}_c$ and an angle γ (Fig. 3), and is given as (in $X_2Y_2Z_2$)

$$g'' = \cos\frac{\gamma}{2} + \frac{\boldsymbol{v}_\gamma}{|\boldsymbol{v}_\gamma|}\sin\frac{\gamma}{2}. \tag{19}$$

The reason why a rotation of g'' in Eq. (18) is required is that the translational tangent displacement changes the direction of normal force and also the direction of $\boldsymbol{f}_s^r$, which should always be vertical to the normal force. Note that translational motion and rotation is completely independent, and one motion does not affect the other. Therefore $\boldsymbol{\tau}_b^r$ and $\boldsymbol{\tau}_t^r$ in Eq. (18) do not need the rotation of g'', similarly $\boldsymbol{f}_s'$ and $\boldsymbol{\tau}'_s$ in Eq. (16) do not need the rotation of g'.

The spring force and torque of each particle are expressed as sums of contributions from all particles bonded to it

$$\boldsymbol{f}_{sp} = \sum q\left(\boldsymbol{f}_r + \boldsymbol{f}_s^t + \boldsymbol{f}_s^r\right) q^{-1}, \tag{20}$$

$$\boldsymbol{\tau}_{sp}^b = \sum\left(\boldsymbol{\tau}_s^t + \boldsymbol{\tau}_s^r + \boldsymbol{\tau}_b^r + \boldsymbol{\tau}_t^r\right). \tag{21}$$

Since $\boldsymbol{f}$ in Eq. (1) is expressed in space-fixed frame, but $\boldsymbol{f}_r$, $\boldsymbol{f}_s^t$ and $\boldsymbol{f}_s^r$ in Eqs. (8), (10) and (18) are evaluated in the body-fixed frame, an extra transfer is required in Eq. (20). Once forces and torques are obtained, Eqs. (1)–(3) can be integrated for each particle.

To test our algorithm described above, we performed simulations where a line of bonded particles is first bended and then twisted. Then we compare the relative errors in the calculation of the total energy incurred using the incremental method (which is used by the most DEMs) and using our algorithm for different time step sizes dt [50]. The relative error is defined as (kinetic energy + potential energy − external work)/(external work). We found that the errors in the incremental method increased much faster with increasing time step than those in our algorithm, indicating that our algorithm is more accurate and stable over a greater range of time step sizes (Fig. 5).

Criterion for bond breakage In the ESyS_Particle model, a bond breaks under either of the following conditions:

If the pure extensional force exceeds the threshold $f_r \geq F_{r0}$ (but it does not break under pure compression)

If the pure tangent force $|f_s| \geq F_{s0}$

If the pure torsional torque $|\tau_t| \geq \Gamma_{t0}$

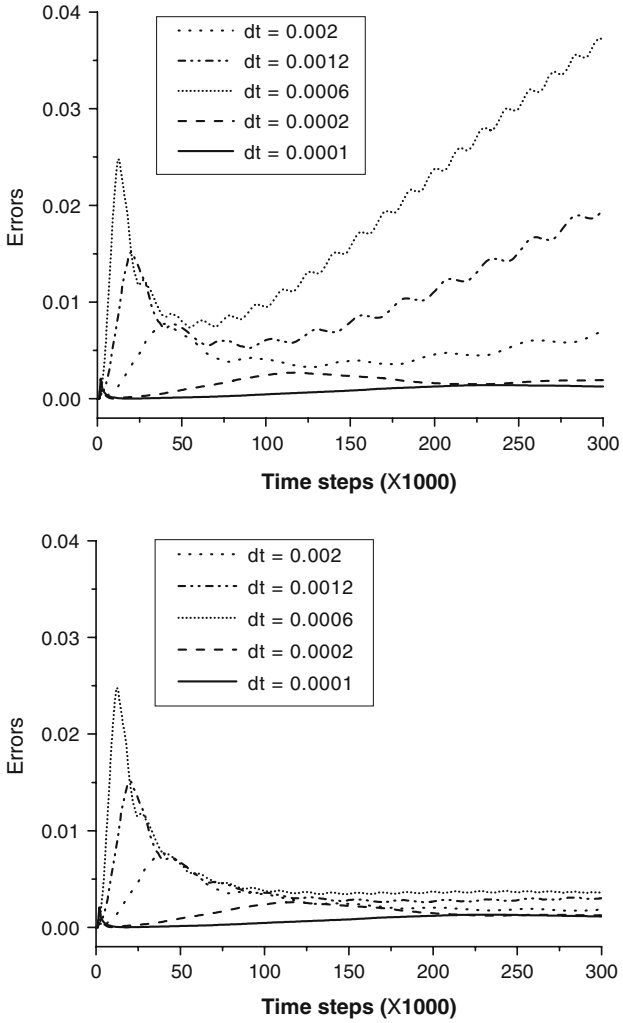

Fig. 5 Evolution of relative errors with time in the incremental method (*top*) and in our algorithm (*bottom*) for different integration time steps dt (from 0.0001 to 0.002). The errors increase much faster in the incremental method than that in our algorithm with increasing integration time step *dt*

If the pure rolling torque $|\tau_b| \geq \Gamma_{b0}$.

When all the interactions exist at the same time, the following empirical criterion is used to judge whether or not a bond is going to break

$$\frac{f_r}{F_{r0}} + \frac{|f_s|}{F_{s0}} + \frac{|\tau_t|}{\Gamma_{t0}} + \frac{|\tau_b|}{\Gamma_{b0}} \geq 1, \tag{22}$$

where $\boldsymbol{f}_s = \boldsymbol{f}_s^t + \boldsymbol{f}_s^r$ (in 3-D). In the 2-D case the third term in Eq. (22) drops. We set f_r positive under extension and negative under compression such that it is more difficult for a bond to break under compression than under extension, and the effects of normal force on breakage of the bond has been taken into account.

The similar combined criteria can be found in [1] where only the first two terms in Eq. (22) are used and in [17] where only the first and fourth term exist. A similar but

parabolic-type criterion is employed in [51]. The other widely used criterion is that a bond breaks either when the tensile strength or the shear strength is reached (either $f_r \geq F_{r0}$ or $|f_s| \geq F_{s0}$) [13,14]. Several different criteria are presented in [2,52]. More work is required to compare the different types of criteria.

2.2.2 Solely normal repulsive interaction

When two particles contact elastically, only the normal force exists when $d < R_1 + R_2$, here d is the distance between the two particles, R_1 and R_2 are radii of two particles

2.2.3 Cohesionless frictional interaction

In the case of the frictional interaction, forces are transmitted in both normal and tangential directions when $d < R_1 + R_2$. The normal force is dealt exactly the same way it is dealt in case of the elastic interaction. In tangential direction, stick-slip frictional force is employed in the current ESyS_Particle model [53].

3 Parameter calibration

In this section we introduce a micro-to-macro approach for our model, which allows us to relate the input parameters of our model to the material parameters of the bulk materials. Our input parameters include the particle mass M, radius R, stiffness parameters K_r, K_s, K_b and K_t, fracture parameters F_{r0}, F_{s0}, Γ_{t0} and Γ_{b0}, artificial damping parameters, integration time step and loading rate etc. We derive the relationship between the macroscopic elastic constants and particle scale stiffness in the case of equal sized particles and regular lattices, which will be presented as follows.

3.1 Elastic parameters: spring stiffness

3.1.1 Background theory

The derivation of the spring constant is based on a comparison between the discrete lattice model and the continuum model [32,54,55]. First we let the displacement of every lattice point equal that of a corresponding point in the continuum model, then we choose a unit cell which is a periodically repeating part of the network in both models, lastly we let the energy stored in the unit cell of lattice equal the strain energy stored in the unit cell of the continuum model.

In the 3-D case, the densest packing of equal-sized spheres are hexagonal closed packing (HCP, Fig. 6) and face-centered cubic (FCC, Fig. 7). In both lattices, every sphere is surrounded by twelve spheres. We employ two sets of coordinates, the global system $x_1x_2x_3$ which defines each particle's

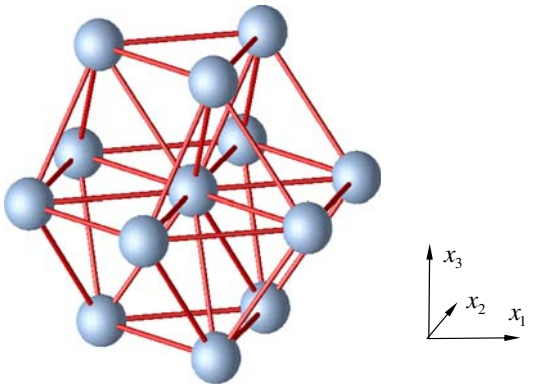

Fig. 6 HCP lattice and coordinate system. The center of the HCP structure is placed on the origin of the coordinates

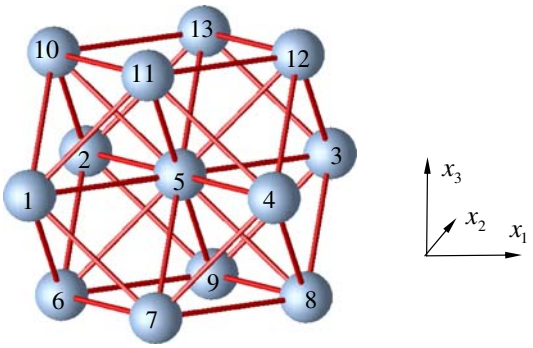

Fig. 7 FCC lattice and coordinate system. The center of the FCC structure is placed on the origin of the coordinates

location, and the local system $x'_1x'_2x'_3$, in which normal and shear displacements are calculated for each bond. $x'_1x'_2x'_3$ is defined by rotating the global system such that x'_3-axis points from the central particle to one of its twelve neighbors (Fig. 8). This rotation is presented by a group of direction cosines: $l_{ij} = \mathbf{cos}(x'_i, x_j)(i, j = 1, 2, 3)$ [56].

Let u_i and u'_i be displacements in the system $x_1x_2x_3$ and $x'_1x'_2x'_3$ respectively. For each particle pair, the derivative of relative displacement in the normal direction is

$$\partial u_r/\partial n = u'_{3,3} = l_{3i}l_{3j}\varepsilon_{ij}, \tag{23}$$

where $\varepsilon_{ij} = (u_{i,j} + u_{j,i})/2$. The derivative of relative displacement in the transverse direction (x'_1-direction and x'_2-direction) are respectively $\partial u_{s1}/\partial n = u'_{1,3} - w'_{13}$, and $\partial u_{s2}/\partial n = u'_{2,3} + w'_{32}$, where $w'_{ij} = (u'_{i,j} - u'_{j,i})/2$ are the contributions from particle rotations. Consider that $u'_j = l_{ji}u_i$ and $\partial/\partial x'_j = l_{ji}\partial/\partial x_i$ we have

$$\partial u_{s1}/\partial n = l_{1i}l_{3j}\varepsilon_{ij} \quad , \partial u_{s2}/\partial n = l_{2i}l_{3j}\varepsilon_{ij} \tag{24}$$

In the case of uniform strain, such as elongation and pure shearing due to loading by a uniform stress, rolling and torsional motions are not involved. We choose the unit cell which is composed of bisecting planes of 12 bonds. The volume of the unit cell is $\Delta V = 4\sqrt{2}\ R^3$, here R is the radius

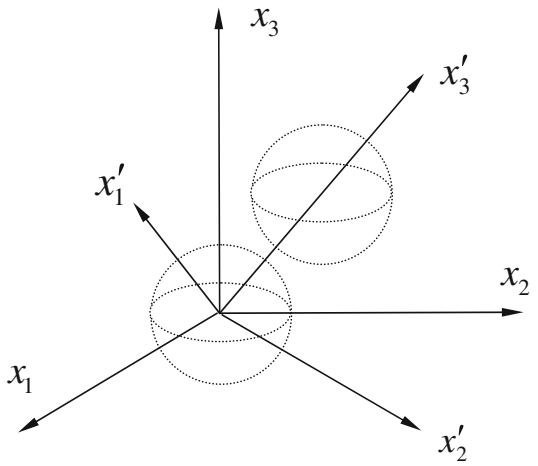

Fig. 8 Global system $x_1x_2x_3$ and local system $x'_1x'_2x'_3$, $x'_1x'_2x'_3$ is gained by rotating the global system such that x'_3-axis points from the central particle to one of its twelve neighbors

of the particles. The elastic energy stored in the unit cell is

$$E_d = R^2 \sum_{i=1}^{12} \left[K_r^i \left(\partial u_r^i / \partial n \right)^2 + K_s^i \left(\partial u_{s1}^i / \partial n \right)^2 + K_s^i \left(\partial u_{s2}^i / \partial n \right)^2 \right]. \tag{25}$$

Letting the strain density $\rho_c = \rho_{dis} = E_d / \Delta V$ and considering $\partial \rho_c / \partial \varepsilon_{ii} = \sigma_{ii}$ and $\partial \rho_c / \partial \varepsilon_{ij} = 2\sigma_{ij}$, the constitutive relation is obtained.

3.1.2 3-D lattices: HCP and FCC

When particles are arranged in HCP lattice (Fig. 6), we have [56]

$$\begin{pmatrix} \sigma_{11} \\ \sigma_{22} \\ \sigma_{33} \\ \sigma_{23} \\ \sigma_{13} \\ \sigma_{12} \end{pmatrix} = \begin{pmatrix} C_{11} & C_{12} & C_{13} & 0 & 0 & 0 \\ C_{12} & C_{11} & C_{13} & 0 & 0 & 0 \\ C_{13} & C_{13} & C_{33} & 0 & 0 & 0 \\ 0 & 0 & 0 & C_{44} & 0 & 0 \\ 0 & 0 & 0 & 0 & C_{44} & 0 \\ 0 & 0 & 0 & 0 & 0 & C_{66} \end{pmatrix} \begin{pmatrix} \varepsilon_{11} \\ \varepsilon_{22} \\ \varepsilon_{33} \\ 2\varepsilon_{23} \\ 2\varepsilon_{13} \\ 2\varepsilon_{12} \end{pmatrix}, \tag{26}$$

where

$$\begin{aligned} C_{11} &= \sqrt{2}\left(29K_r^2 + 89K_s^2 + 170K_rK_s\right)/48R\left(K_r + 5K_s\right), \\ C_{12} &= \sqrt{2}(K_r - K_s)\left(11K_r + 49K_s\right)/48R\left(K_r + 5K_s\right), \\ C_{13} &= \sqrt{2}(K_r - K_s)/6R, \\ C_{33} &= \sqrt{2}(2K_r + K_s)/3R, \\ C_{44} &= \sqrt{2}(K_r + 2K_s)/6R, \\ C_{66} &= \sqrt{2}\left(3K_r^2 + 23K_s^2 + 22K_rK_s\right)/16R\left(K_r + 5K_s\right) \\ &= (C_{11} - C_{12})/2. \end{aligned}$$

This is transversely isotropic, which is a special case of an orthotropic solid [57]. We can write the compliance form of Eq. (26) as

$$\begin{pmatrix} \varepsilon_{11} \\ \varepsilon_{22} \\ \varepsilon_{33} \\ 2\varepsilon_{23} \\ 2\varepsilon_{13} \\ 2\varepsilon_{12} \end{pmatrix} = \begin{pmatrix} 1/E_x & -\nu_{yx}/E_y & -\nu_{zx}/E_z & 0 & 0 & 0 \\ -\nu_{xy}/E_x & 1/E_y & -\nu_{zy}/E_z & 0 & 0 & 0 \\ -\nu_{xz}/E_x & -\nu_{yz}/E_y & 1/E_z & 0 & 0 & 0 \\ 0 & 0 & 0 & 1/\mu_{yz} & 0 & 0 \\ 0 & 0 & 0 & 0 & 1/\mu_{xz} & 0 \\ 0 & 0 & 0 & 0 & 0 & 1/\mu_{xy} \end{pmatrix} \times \begin{pmatrix} \sigma_{11} \\ \sigma_{22} \\ \sigma_{33} \\ \sigma_{23} \\ \sigma_{13} \\ \sigma_{12} \end{pmatrix}$$

The Young's modulus, Poisson's ratio and shear modulus are respectively

$$\begin{aligned} E_x &= E_y = \frac{3\sqrt{2}K_r\left(K_r + K_s\right)\left(3K_r^2 + 23K_s^2 + 22K_rK_s\right)}{R\left(18K_r^3 + 119K_r^2K_s + 128K_rK_s^2 + 23K_s^3\right)}, \\ E_z &= \frac{3\sqrt{2}K_r\left(K_r + K_s\right)}{R\left(5K_r + K_s\right)}, \\ \nu_{xy} &= \nu_{yx} = \frac{\left(K_r - K_s\right)\left(6K_r^2 + 23K_s^2 + 31K_rK_s\right)}{18K_r^3 + 119K_r^2K_s + 128K_rK_s^2 + 23K_s^3}, \\ \nu_{zx} &= \nu_{zy} = \frac{K_r - K_s}{5K_r + K_s}, \\ \nu_{xz} &= \nu_{yz} = \frac{\left(K_r - K_s\right)\left(3K_r^2 + 23K_s^2 + 22K_rK_s\right)}{18K_r^3 + 119K_r^2K_s + 128K_rK_s^2 + 23K_s^3}, \\ \mu_{xy} &= \frac{\sqrt{2}\left(3K_r^2 + 23K_s^2 + 22K_rK_s\right)}{16R\left(K_r + 5K_s\right)}, \\ \mu_{xz} &= \mu_{yz} = \frac{\sqrt{2}\left(K_r + 2K_s\right)}{6R}. \end{aligned} \tag{27}$$

Similarly in the case of FCC (Fig. 7), we have [56]

$$\begin{pmatrix}\sigma_{11}\\ \sigma_{22}\\ \sigma_{33}\\ \sigma_{23}\\ \sigma_{13}\\ \sigma_{12}\end{pmatrix}=\begin{pmatrix}C_{11} & C_{12} & C_{12} & 0 & 0 & 0\\ C_{12} & C_{11} & C_{12} & 0 & 0 & 0\\ C_{12} & C_{12} & C_{11} & 0 & 0 & 0\\ 0 & 0 & 0 & C_{44} & 0 & 0\\ 0 & 0 & 0 & 0 & C_{44} & 0\\ 0 & 0 & 0 & 0 & 0 & C_{44}\end{pmatrix}\begin{pmatrix}e_{11}\\ e_{22}\\ e_{33}\\ 2e_{23}\\ 2e_{13}\\ 2e_{12}\end{pmatrix}\quad\text{and}$$

$$\begin{pmatrix}\varepsilon_{11}\\ \varepsilon_{22}\\ \varepsilon_{33}\\ 2\varepsilon_{23}\\ 2\varepsilon_{13}\\ 2\varepsilon_{12}\end{pmatrix}=\begin{pmatrix}1/E & -\nu/E & -\nu/E & 0 & 0 & 0\\ -\nu/E & 1/E & -\nu/E & 0 & 0 & 0\\ -\nu/E & -\nu/E & 1/E & 0 & 0 & 0\\ 0 & 0 & 0 & 1/\mu & 0 & 0\\ 0 & 0 & 0 & 0 & 1/\mu & 0\\ 0 & 0 & 0 & 0 & 0 & 1/\mu\end{pmatrix}\begin{pmatrix}\sigma_{11}\\ \sigma_{22}\\ \sigma_{33}\\ \sigma_{23}\\ \sigma_{13}\\ \sigma_{12}\end{pmatrix}, \tag{28}$$

where $C_{11}=\sqrt{2}\,(K_r+K_s)/2R$, $C_{12}=\sqrt{2}\,(K_r-K_s)/4R$ and $C_{44}=\sqrt{2}(K_r+K_s)/4R=C_{11}/2$. From Eq. (28), we know that this is cubic material, the simplest case for an orthotropic solid [57]. Three independent macroscopic elastic constants are

$$\begin{aligned}E&=\frac{\sqrt{2}\,(K_r+3K_s)\,K_r}{R\,(3K_r+K_s)},\\ \nu&=\frac{K_r-K_s}{3K_r+K_s},\\ \mu&=\frac{\sqrt{2}\,(K_r+K_s)}{4R}.\end{aligned} \tag{29}$$

K_r and K_s can be expressed in terms of E and ν as follows:

$$K_r=\frac{\sqrt{2}ER}{2\,(1-2\nu)},\quad K_s=\frac{1-3\nu}{1+\nu}K_r. \tag{30}$$

To have an estimation of K_b and K_t, we consider an infinite FCC continuum subjected to the pure bending stress: $\sigma_{11}=Hz, \sigma_{22}=\sigma_{33}=0, \sigma_{12}=\sigma_{23}=\sigma_{13}=0$. Here H is a small constant. This stress field corresponds to macroscopic bending.

In this case, rotation is involved. In the local system $x'_1x'_2$ x'_3, the rotations of particles around three axes are represented by

$$w'_{ij}=\left(u'_{i,j}-u'_{j,i}\right)/2=l_{i\alpha}l_{j\beta}w_{\alpha\beta}, \tag{31}$$

where $w_{\alpha\beta}=(u_{\alpha,\beta}-u_{\beta,\alpha})/2$. Then the relative torsional angle around x'_3-axis and the two bending angles around x'_1- and x'_2- axis are respectively (under small deformation assumption)

$$\begin{aligned}&\Delta\theta_t=w'_{21B}-w'_{21A},\ \Delta\theta_{b1}=w'_{32B}-w'_{32A},\\ &\Delta\theta_{b2}=w'_{13B}-w'_{13A}.\end{aligned} \tag{32}$$

By comparing the strain energy distribution and the distribution of moments with respect to the y axis between the continuum model and discrete lattice model, we have [56]

$$\begin{aligned}K_b&=\frac{\sqrt{2}ER^3}{48\,(1-\nu)}=\frac{(1-2\nu)\,R^2}{24\,(1-\nu)}K_r,\\ K_t&=\frac{1-3\nu}{1+\nu}K_b=\frac{(1-2\nu)\,R^2}{24\,(1-\nu)}K_s.\end{aligned} \tag{33}$$

Equation (33) is among the rare attempts to estimate the rotational stiffness besides Chang [37]. However, there are some fundamental differences between our derivations of Eq. (33) and those of Chang's. First, their study is concerned with the derivation of macroscopic elastic parameters from the given particle scale spring stiffnesses (i.e. K_r, K_s, K_b and K_t). In contract, our studies follow the reverse direction, that is, we derive the particle scale spring stiffness (K_r, K_s, K_b and K_t) from the given macroscopic elastic parameters (i.e. E and ν). Second, in Chang's micropolar theory, the rotational stiffnesses K_b and K_t are related to three additional parameters (or polar constants), therefore they are independent of K_r and K_s(or E and ν), and may approach infinity. In our formulas, K_b and K_t can not be infinite large, instead they are related to K_r and K_s (or E and ν). The reason behind this disagreement is that our purpose is to reproduce the equivalent macroscopic continuum elasticity, rather than elasticity with strong micro-polar effect.

3.1.3 2-D triangular lattice

For the 2-D triangular lattice, Eq. (4) is reduced to $f_r=K_r\Delta r$, $f_s=K_s\Delta s$, and$\tau_b=K_b\Delta\alpha_b$. Similarly we have [56]

$$K_r=\frac{\sqrt{3}E}{3\,(1-\nu)},\quad K_s=\frac{1-3\nu}{1+\nu}K_r. \tag{34}$$

It generates macroscopic isotropic elasticity if we assume the spring constants are identical for all bonds. This means that Eq. (34) is invariant with respect to α, the orientation of the lattice (Fig. 9). The bending stiffness is determined similarly

$$K_b=\frac{\sqrt{3}\,(1+\nu)\,(1-2\nu)\,ER^2}{36\,(1-\nu)}. \tag{35}$$

4 Numerical validations

The analytical results of Eqs. (30) and (33) have been tested numerically using a 3-D FCC block under uni-axial compression [56]. We change the tangent stiffnessK_s, and plot the computed νagainst K_s/K_r in Fig. 10. The dots correspond to the measurements from the numerical simulations, and the line is the analytical result $\nu=(1-\beta)/(3+\beta)$ (from the second equation term in Eq. (30)), here $\beta=K_s/K_r$. The close agreement between the numerical measurements and the analytical line validates the analytical results.

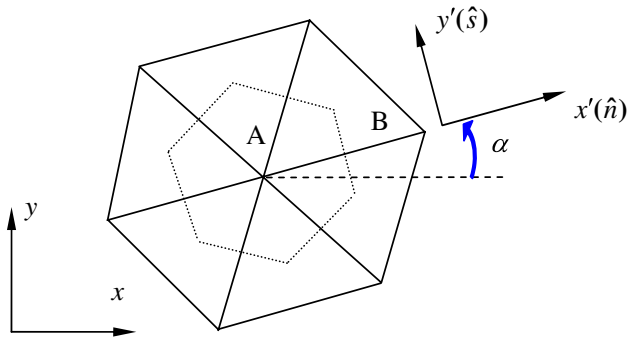

Fig. 9 2D close-packed hexagonal lattice and unit cell (the area enclosed by dashed lines)

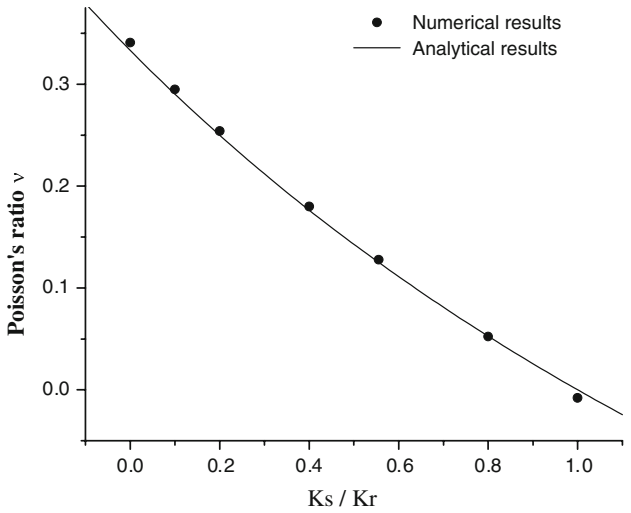

Fig. 10 The variations of Poisson's ratio with K_s/K_r. The analytical line is $\nu = (1-\beta)/(3+\beta)$, here $\beta = K_s/K_r$

Some numerical simulations of rock fracture are performed using ESyS_Particle code. Figure11 shows the 2-D wing crack extensions simulations. Wing cracks are frequently observed in uni-axial compression of brittle materials with a pre-existed crack. The typical growth pattern of wing cracks is that tensile cracks nucleate at the tips of the flaw, grow in a stable manner with increasing of compression, then tend to align with the direction of axial loads [58]. The most basic features of the laboratory observations are reproduced (Fig. 11, left).

It is also found that if the single particle rotation is prohibited, or rolling stiffness between particles is absent (Fig. 11, right), the realistic pattern of crack propagation observed in laboratories can not be reproduced. Only when normal, tangent and rolling stiffness exist and particle rotation is permitted (Fig. 11, left), is it possible to reproduce laboratory tests [59]. We conclude that particle rotation and rolling resistance play a significant role and can not be neglected while modeling such phenomenon.

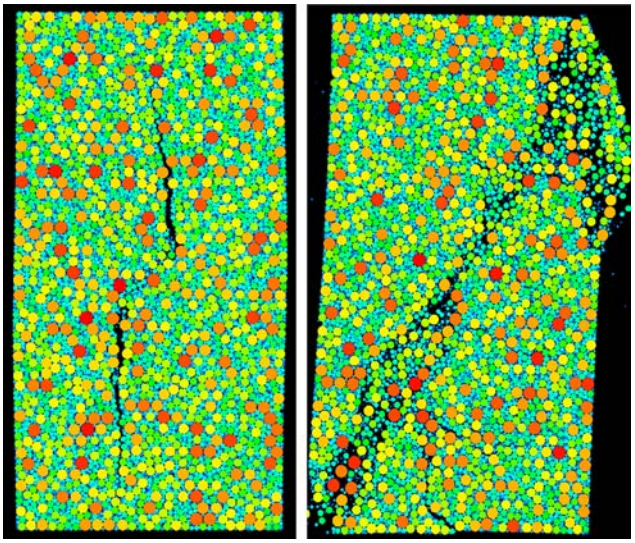

Fig. 11 Simulations of 2-D wing crack extension. *Left* results with rolling resistance, *right* results without rolling resistance

Figure 12 shows the progressive fractures in a 3-D brittle rock-like material. In this example, equal-sized particles are arranged into FCC lattice which is subjected to a slow uniaxial compression in vertical direction. The colors represent vertical displacement. Discontinuities mean the formation of fractures which is difficult to be captured in laboratory tests since this process always occurs very fast. After the peak stress, the main faults are formed quickly and two intact cores can be clearly observed with more fragile parts shattering away from four sides. This kind of pattern is always observed in rock fracture tests. Although this preliminary simulation is obtained using a regular packing, which is not yet a realistic representation of geo-materials, it reproduces the most important features of brittle fracture, such as the brittle behavior and two intact cores. Further studies are going to be done for the different sized particle packing.

5 Discussions and conclusions

We present our DEM model, in which six parameters are used to describe a single 3-D rigid body and each rigid body is permitted to rotate. Neighboring bodies can be bonded together by springs which transmit a full set of interactions. Our model and algorithms are original with respect to some existing algorithms in the following aspects: Firstly we use quaternion to represent 3-D particle orientation into a finite deformation scheme. There are no explicit rotational degrees of freedom for particles in some of existing models, instead only three angular velocities around three orthogonal axes are used. In the 3-D case, one can not extract the exact orientation

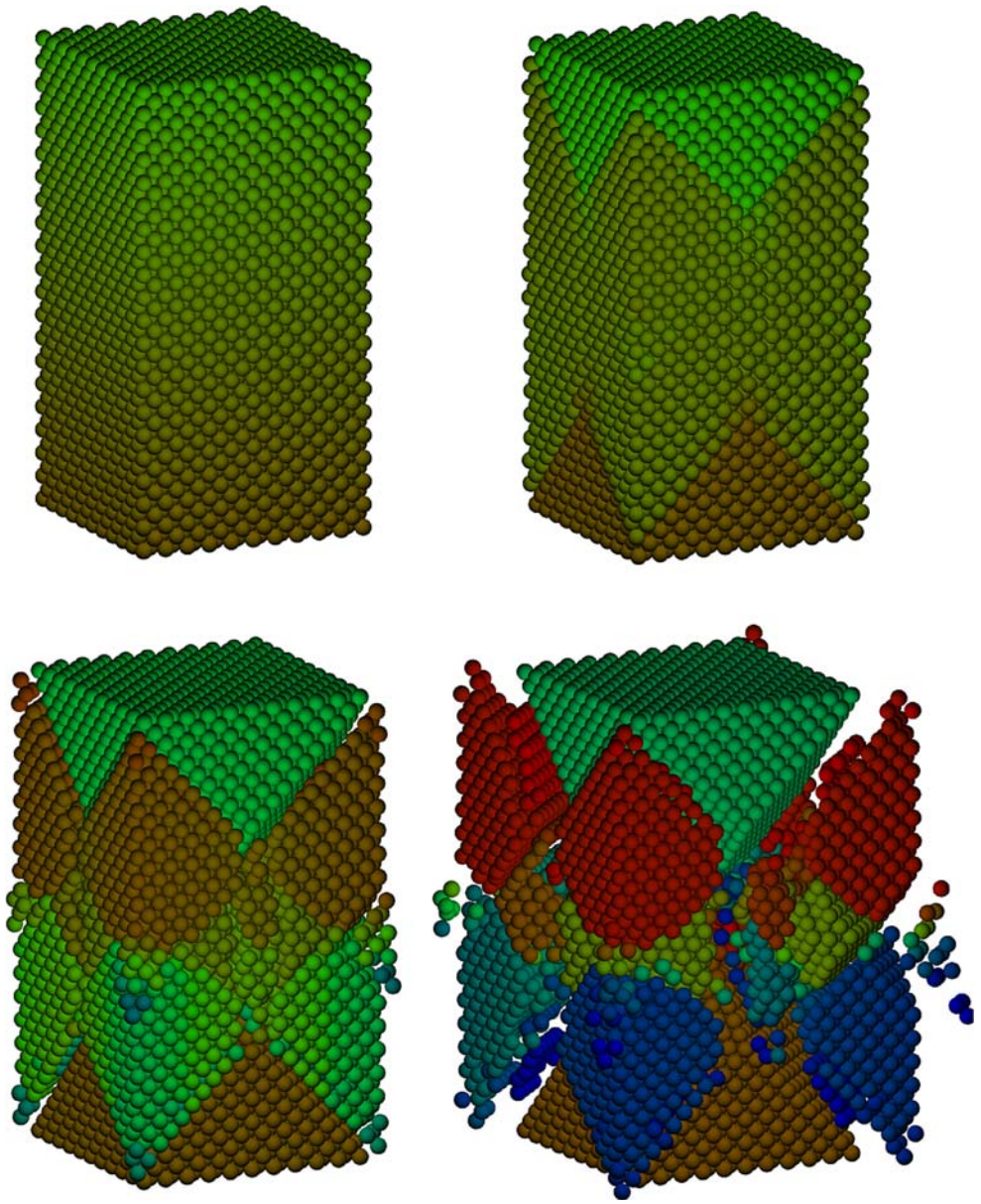

Fig. 12 Progressive fractures in 3D brittle rock under uni-axial compression

for each particle by simply integrating from the three angular velocities, the reason is that even if three angles are obtained by integration, the exact orientation of a particle still can not be uniquely decided, since *finite rotations in 3-D are order dependent.* In other words, for the same three angles, different sequences of rotations will result in different final orientations.

Secondly, our algorithm is based on the finite deformation method in which total displacements are calculated instead of the incremental displacements. At each time step $T = t$, we only need initial, current position and orientation (i.e. at $T = 0$ and t). In the most existing algorithms, force and torques are computed in an incremental fashion. This means that three incremental angles from time *t-dt* to *t* are computed using three angular velocities, and then three incremental torques are calculated and added to the torques at time *t-dt* to get the torques at time *t*. The orders of the three incremental rotations are ignored, which is theoretically permitted only in case of infinitesimal rotations. It should be pointed out that when torsion and rolling co-exist, rolling changes the axis of torsion (Fig. 4), the incremental method failed to decouple them. Using our decomposition technique, rolling and torsion are completely decoupled and uniquely determined, and so are forces and torques between particles. Our algorithm is numerically more accurate than the incremental method and physically reliable. It is also very reliable when torsion

and rolling stiffness are different and total potential energy is required.

Lastly, theoretically only infinitesimal rotations in 3-D are order independent, this means that the incremental method requires very small time steps, therefore errors in the incremental method increase faster than in our algorithm as the time step increases (Fig. 5).

We derived elastic parameters for the regular lattice model in 2-D and 3-D. The results suggest that in the 2-D case, the closely packed hexagonal lattice generates macroscopic isotropic elasticity if we assume the spring constants are identical for all bonds. While in the 3-D case, the densest packing, HCP and FCC lattice, generate anisotropic elasticity. This means that one must be careful defining how the coordinate system is chosen when referring to Eqs. (26) and (28). Our study also show that generally the ratio of the tangent to the normal stiffness determines Poisson's ratioν, and only when $K_r = K_s$ (which leads to $\nu = 0$) do HCP and FCC yield isotropic material. We suggest that $K_s \leq K_r$ should be used as an upper limitation for K_s in DEM simulations.

From Eqs. (33) and (35), we know that $K_b \propto ER^2$ in the 2-D case, and $K_t, K_b \propto ER^3$ in the 3-D case, this implies that when the particle size approaches zero the effects of the rotational stiffness on the macroscopic elasticity can be neglected. However their contribution to failure criterion and effect in local stress transfer can not be ignored, as shown in the wing crack simulation [59]. It should be pointed out that Eqs. (26)–(30) and (33)–(35) are obtained under assumption of equal-sized particle and regular packing, for the random packing with different particle sizes, the stiffnesses need to be changed for each particle pairs according to the radii of the particles. In spite of this, Eqs. (26)–(30) and (33)–(35) can still be used as a theoretical basis for the choice of parameters in DEM modeling.

Acknowledgments We would like to thank Alina Hale for writing corrections. Yucang Wang acknowledges the support of the ACcESS and AuScope project. Fernando Alonso-Marroquin is supported by the Australian Research Council and the University of Queensland's Early Carrier Research Grant.

References

1. Cundall, P.A., Stack, O.D.L.: A discrete numerical model for granular assemblies. Geotechnique **29**, 47–65 (1979)
2. Luding, S.: Cohesive, frictional powders: contact mode for tension. Granul. Matter **10**, 235–246 (2008). doi:10.1007/s10035-008-0099-x
3. Mora, P., Place, D.: A lattice solid model for the nonlinear dynamics of earthquakes. Int. J. Mod. Phys. **C4**, 1059–1074 (1993)
4. Mora, P., Place, D.: Simulation of the friction stick-slip instability. Pure Appl. Geophys. **143**, 61–87 (1994). doi:10.1007/BF00874324
5. Mora, P., Place, D.: Numerical simulation of earthquake faults with gouge: towards a comprehensive explanation for the heat flow paradox. J. Geophys. Res. **103**, 21067–21089 (1998). doi:10.1029/98JB01490
6. Place, D., Mora, P.: A lattice solid model to simulate the physics of rocks and earthquakes: incorporation of friction. J. Comput. Phys. **150**, 332–372 (1999). doi:10.1006/jcph.1999.6184
7. Place, D., Lombard, F., Mora, P., Abe, S.: Simulation of the micro-physics of rocks using LSMearth. Pure Appl. Geophys. **159**, 1933–1950 (2002). doi:10.1007/s00024-002-8715-x
8. Toomey, A., Bean, C.J.: Numerical simulation of seismic waves using a discrete particle scheme. Geophys. J. Int. **141**, 595–604 (2000)
9. Chang, S.H., Yun, K.J., Lee, C.I.: Modeling of fracture and damage in rock by the bonded-particle model. Geosyst. Eng. **5**, 113–120 (2002)
10. Hazzard, J.F., Collins, D.S., Pettitt, W.S., Young, R.P.: Simulation of unstable fault slip in granite using a bonded-particle model. Pure Appl. Geophys. **159**, 221–245 (2000a). doi:10.1007/PL00001252
11. Hazzard, J.F., Young, R.P.: Simulation acoustic emissions in bonded-particle models of rock. Int. J. Rock Mech. Min. Sci. **37**, 867–872 (2002)
12. Potyondy, D., Cundall, P., Lee, C.A.: Modelling rock using bonded assemblies of circular particles. In: Hassani, F., Mitri, H. (eds.) Rock Mechanics. Balkema, Rotterdam (1996)
13. Potyondy, D., Cundall, P.: A bonded-particle model for rock. Int. J. Rock Mech. Min. Sci. **41**, 1329–1364 (2004). doi:10.1016/j.ijrmms.2004.09.011
14. Donze, F.V., Bouchez, J., Magnier, S.A.: Modeling fractures in rock blasting. Int. J. Rock Mech. Min. Sci. **34**, 1153–1163 (1997). doi:10.1016/S0148-9062(97)00300-8
15. Hentz, S., Daudeville, L., Donze, F.V.: Identification and validation of a discrete element model for concrete. J. Eng. Mech. **130**, 709–719 (2004a). doi:10.1061/(ASCE)0733-9399(2004)130:6(709)
16. Hentz, S., Donze, F.V., Daudeville, L.: Discrete Element modeling of concrete submitted to dynamics loading at high strain rates. Comput. Struc. **82**, 2509–2524 (2004b). doi:10.1016/j.compstruc.2004.05.016
17. Kun, F., Herrmann, H.J.: A study of fragmentation process using a discrete element method. Comput. Methods Appl. Mech. Eng. **138**, 3–18 (1996). doi:10.1016/S0045-7825(96)01012-2
18. Scott, D.: Seismicity and stress rotation in a granular model of the brittle crust. Nature **381**, 592–595 (1996). doi:10.1038/381592a0
19. Wang, Y.C., Yin, X.C., Ke, F.J., Xia, M.F., Peng, K.Y.: Numerical simulation of rock failure and earthquake process on mesoscopic scale. Pure Appl. Geophys. **157**, 1905–1928 (2000). doi:10.1007/PL00001067
20. Alonso-Marroquin, F., Vardoulakis, I., Herrmann, H.J., Weatherley, D., Mora, P.: The effect of rolling on dissipation in fault gouges. Phys. Rev. E Stat. Nonlin. Soft Matter Phys. **74**(1), 031306 (2006). doi:10.1103/PhysRevE.74.031306
21. Oda, M., Konishi, J., Nemat-Nasser, S.: Experimental micromechanical evaluation of the strength of granular materials: effects of particle rolling. Mech. Mater. **1**, 269–283 (1982). doi:10.1016/0167-6636(82)90027-8
22. Oda, M., Kazama, H.: Microstructure of shear bands and its relation to the mechanisms of dilatancy and failure of dense granular soils. Geotechnique **48**(4), 465–481 (1998)
23. Oda, M., Iwashita, K.: Study on couple stress and shear band development in granular media based on numerical simulation analyses. Int. J. Eng. Sci. **38**, 1713–1740 (2000). doi:10.1016/S0020-7225(99)00132-9
24. Iwashita, K., Oda, M.: Rolling resistance at contacts in simulation of shear band development by DEM. J. Eng. Mech. **124**, 285–292 (1998). doi:10.1061/(ASCE)0733-9399(1998)124:3(285)
25. Iwashita, K., Oda, M.: Micro-deformation mechanism of shear banding process based on modified distinct element

method. Powder Technol. **109**, 192–205 (2000). doi:10.1016/S0032-5910(99)00236-3
26. Kuhn, M.R., Bagi, K.: Contact rolling and deformation in granular media. Int. J. Solids Struct. **41**, 5793–5820 (2004). doi:10.1016/j.ijsolstr.2004.05.066
27. Tordesillas, A., Walsh, D.C.S.: Incorporating rolling resistance and contact anisotropy in micromechanical models of granular media. Powder Technol. **124**, 106–111 (2002). doi:10.1016/S0032-5910(01)00490-9
28. Sakaguchi, H., Muhlhaus, H.: Hybrid modeling of coupled pore fluid-solid deformation problems. Pure Appl. Geophys. **157**, 1889–1904 (2000). doi:10.1007/PL00001066
29. Boutt, D.F., McPherson, B.J.O.L.: Simulation of sedimentary rock deformation: lab-scale model calibration and parameterization. Geophys. Res. Lett. **29** (2002). doi:10.1029/2001GL013987
30. Matsuda, Y., Iwase, Y.: Numerical simulation of rock fracture using three-dimensional extended discrete element method. Earth Planets Space. **54**, 367–378 (2002)
31. Walton, K.: The effective elastic moduli of a random packing of spheres. J. Mech. Phys. Solids **35**, 213–226 (1987). doi:10.1016/0022-5096(87)90036-6
32. Bathurst, R.J., Rothenburg, L.: Micromechanical aspects of isotropic granular assemblies with linear contact interactions. J. Appl. Mech. **55**, 17–23 (1988)
33. Deresiewicz, H.: Stress–strain relations for a simple model of a granular medium. J. Appl. Mech. **25**(3), 402–406 (1958)
34. Duffy, J., Mindlin, R.D.: Stress–strain relations and vibrations of a granular medium. J. Appl. Mech. **24**(4), 585–593 (1957)
35. Duffy, J.: A differential stress–strain relation for the hexagonal close-packed array of elastic spheres. J. Appl. Mech. **26**, 88–94 (1959)
36. Walton, K.: The effective elastic moduli of model sediments. Geophys. J. R. **43**, 293–306 (1975)
37. Chang, C.S., Gao, J.: Kinematic and static hypotheses for constitutive modeling of granulates considering particle rotation. Acta Mech. **115**, 213–229 (1996). doi:10.1007/BF01187439
38. Allen, M.P., Tildesley, D.J.: Computer Simulation of Liquids. Oxford Science Press, Oxford (1987)
39. Rapaport, D.C.: The Art of Molecular Dynamic Simulation. Cambridge University press, Cambridge (1995)
40. Mora, P., Place, D.: The weakness of earthquake faults. Geophys. Res. Lett. **26**, 123–126 (1999)
41. Place, D., Mora, P.: Numerical simulation of localization in a fault zone. Pure Appl. Geophys. **157**, 1821–1845 (2000). doi:10.1007/PL00001063
42. Mora, P., Wang, Y.C., Yin, C., Place, D.: Simulation of the load-unload response ratio and critical sensitivity in the lattice solid model. Pure Appl. Geophys. **159**, 2525–2536 (2002). doi:10.1007/s00024-002-8746-3
43. Wang, Y.C., Mora, P., Yin, C., Place, D.: Statistical tests of load-unload response ratio signals by lattice solid model: implication to tidal triggering and earthquake prediction. Pure Appl. Geophys. **161**, 1829–1839 (2004)
44. Mora, P., Place, D.: Stress correlation function evolution in lattice solid elasto-dynamic model of shear and fracture zones and earthquake prediction. Pure Appl. Geophys. **159**, 2413–2427 (2002). doi:10.1007/s00024-002-8741-8
45. Goldstein, H.: Classical Mechanics, 2nd edn. Addison-Wesley, Reading (1980)
46. Evans, D.J.: On the representation of orientation space. Mol. Phys. **34**, 317–325 (1977). doi:10.1080/00268977700101751
47. Evans, D.J., Murad, S.: Singularity free algorithm for molecular dynamic simulation of rigid polyatomice. Mol. Phys. **34**, 327–331 (1977). doi:10.1080/00268977700101761
48. Kuipers, J.B.: Quaternions and Rotation Sequences. Princeton University Press, Princeton (1998)
49. Wang, Y.C., Abe, S., Latham, S., Mora, P.: Implementation of particle-scale rotation in the 3D lattice solid model. Pure Appl. Geophys. **163**, 1769–1785 (2006). doi:10.1007/s00024-006-0096-0
50. Wang, Y.C.: A complete scheme for modeling 3D interactive rigid body motion with six degrees of freedom and full rigidity. Acta Geotech. (2009) (in press). doi:10.1007/s11440-008-0072-1
51. Pelenne, J.Y., Youssoufi, M.S.E., Cherblanc, F., Benet, J.C.: Mechanical behviour and failure of cohesive granular materials. Int. J. Numer. Anal. Mech. Geomech. **28**, 1577–1594 (2004). doi:10.1002/nag.401
52. Davie, C.T., Bicanic, N.: Failure criteria for qusi-brittle materials in lattice-type models. Commun. Numer. Methods Eng. **19**, 703–713 (2003). doi:10.1002/cnm.626
53. Wang, Y.C., Mora, P.: ESyS_Particle: A new 3-D discrete element model with single particle rotation. In: Xing, H.L. (ed.) Advances in Geocomputing. Springer, pp. 183–228 (2009)
54. Griffiths, D.V., Mustoe, G.G.W.: Modeling of elastic continuum using a grillage of structural elements based on discrete element concepts. Int. J. Numer. Methods Eng. **50**, 1759–1775 (2001). doi:10.1002/nme.99
55. Ostoja-Starzewski, M.: Lattice models in micromechanics. Appl. Mech. Rev. **55**, 35–60 (2002). doi:10.1115/1.1432990
56. Wang, Y.C., Mora, P.: Elastic properties of regular lattices and calibration of 3-D Discrete Element Model. J. Mech. Phys. Solids **56**, 3459–3474 (2008). doi:10.1016/j.jmps.2008.08.011
57. Daniel, I.M., Ishai, O.: Engineering mechanics of composite material. Oxford University Press, Oxford (1994)
58. Brace, W.F., Bombolakis, E.G.: A note on brittle crack growth in compression. J. Geophys. Res. **68**, 3709–3713 (1963). doi:10.1029/JZ068i012p03709
59. Wang, Y.C., Mora, P.: Modeling wing crack extension: implications to the ingredients of discrete element model. Pure Appl. Geophys. **165**, 609–620 (2008). doi:10.1007/s00024-008-0315-y